Atmos. Meas. Tech. Discuss., 5, 8815–8838, 2012
www.atmos-meas-tech-discuss.net/5/8815/2012/
doi:10.5194/amtd-5-8815-2012

Atmospheric Measurement Techniques Discussions

Feasibility of polarized all-sky imaging for aerosol characterization

A. Kreuter and M. Blumthaler

Division for Biomedical Physics, Department of Physiology and Medical Physics, Innsbruck Medical University, Muellerstr. 44, 6020 Innsbruck, Austria

Received: 15 November 2012 – Accepted: 6 December 2012 – Published: 14 December 2012

Correspondence to: A. Kreuter (axel.kreuter@i-med.ac.at)

Published by Copernicus Publications on behalf of the European Geosciences Union.

Abstract

Polarized all-sky distribution measurements contain radiative information about aerosol properties. We investigate the method of all-sky imaging for aerosol property retrieval and propose a technical frame work for image processing and analysis. Using Zernike polynomials, we decompose the relative Stokes parameter distributions, which efficiently captures the information content. The resulting feature vector is well suited for all-sky imaging, independent of calibration and robust against noise. It can be directly used in existing algorithms or alternative types of retrieval methods of aerosol optical properties in the future. By modeling possible aerosol scenarios we investigate the influence of different aerosol types in terms of the first two principal components describing the maximal variances. In this representation we show that the feature vector from a polarized all-sky imager is suitable for aerosol classification with respect to size and single scatter albedo.

1 Introduction

Aerosols in the atmosphere absorb and scatter solar radiation and hence modify the earth's radiation budget. In addition to this direct effect, several indirect effects involving cloud formation add to the aerosols' complex impact on climate that are relatively poorly understood (Forster et al., 2007). One important step towards a better representation of aerosols in future climate models is to improve global aerosol characterization from the observational side.

Aerosol distribution and properties may vary strongly on both temporal and spatial scales, so satellite observations of aerosols would be ideally suited (Kaufman et al., 2002). However, these measurements are limited by ground albedo and ground based remote sensing remains a key method to determine the aerosol properties by remote sensing.

AMTD
5, 8815–8838, 2012

The physical observable in remote sensing is the radiance, which is measured in different viewing angles (distribution), wavelength bands and includes the polarization state. The radiance distribution is commonly measured with sky scanning radiometers with a small field-of-view input optics pointing at discrete viewing angles. Typically, two specific sections in the sky are measured: the principal plane (PP), the vertical plane containing the sun and the zenith. The so-called almucantar is a scan of the azimuth angle at a constant elevation angle of the sun, the solar zenith angle (SZA).

These measurements constitute the input data for retrieval schemes for aerosol optical properties, such as the one used for the Aerosol Robotic Network (AERONET) (Holben et al., 1998; Dubovik et al., 2000). Since aerosol scattering alters not only the sky radiance but also its polarization, polarization adds independent measurement degrees of freedom with respect to aerosols (e.g. Vermeulen et al., 2000; Boesche et al., 2006; Li et al., 2009).

Here we want to explore an alternative method of measuring the sky radiance: all-sky imaging, i.e. projecting the polarized sky hemisphere onto a camera chip (see e.g. North and Duggin, 1997; Liu and Voss, 1997; Pust and Shaw, 2008; Cazorla et al., 2009; Kreuter et al., 2009). This approach has the distinct advantage of data acquisition speed – the whole distribution in multiple wavelengths bands is captured in one exposure. The data also contain versatile information with meteorological relevance, such as cloud cover which is important for the retrieval accuracy of aerosol properties, as the general assumption is a clear sky.

The main disadvantage of all-sky imaging is that the area around the sun, the aureole, cannot be resolved satisfactorily. Wavelength resolution is typically broadband, as most commercial sensors aim at reproducing a physiological color image (RGB). Furthermore, these sensors are not optimized for absolute radiometric stability.

AMTD
5, 8815–8838, 2012

2 Method

2.1 Data and simulations

The (linearly) polarized sky radiance is described by the three Stokes parameters I, Q and U. The Stokes parameters from all viewing directions in the sky hemisphere produce the polarized sky radiance distribution, which we will simply call Stokes maps.

Methodologically, in all-sky imaging, the entire distribution is captured in a single exposure by a fisheye projection (an equiangular projection, mapping the sky's hemisphere onto a circular disk in a photo). For each pixel, the Stokes parameters are determined according to the operational Stokes-vector definition (e.g. Born and Wolf, 1999):

$$\begin{pmatrix} I \\ Q \\ U \end{pmatrix} = \begin{pmatrix} I_0 + I_{90} \\ I_0 - I_{90} \\ I_{45} - I_{135} \end{pmatrix} \quad (1)$$

where the subscripts denote relative polarizer orientations with respect to an arbitrary reference angle. So experimentally, four images at four different polarizer orientations separated by 45° are required. The method is presented in more detail in (Kreuter et al., 2009).

For the purpose of this study, we simulate Stokes maps for different aerosol scenarios using Model calculations. The model we use is the Monte Carlo radiative transfer model MYSTIC which is planned to be publicly available in a future release of the libRadtran Package (Mayer and Kylling, 2005). The MYSTIC solver has been extensively validated and is described by (Mayer, 2009, and Emde et al., 2010). Here we use a simplified 1-D version of MYSTIC, with the restriction of a homogeneous and flat surface, with ground albedo set to zero throughout this study.

As the model input, in addition to the standard atmospheric input parameters (atmospheric profile, etc.) the aerosol characteristics are specified using the OPAC database

AMTD
5, 8815–8838, 2012

for aerosol optical properties (Hess et al., 1998). For our purposes here, we only consider two wavelengths, 450 nm and 650 nm, roughly corresponding to the center wavelengths of the blue (B) and red (R) channels of typical RGB sensors.

All simulations shown here are performed with 3×10^4 photons resulting in a standard deviation of less than 1 % in the radiance. The viewing angle grid is set up in Cartesian coordinates (rather than radial) to produce a constant solid angle for each pixel. Each map consists of 901 viewing directions, with a FOV of 5°. An example of Stokes maps at solar zenith angle (SZA) of 60°, wavelength of 650 nm and an aerosol of OPAC-type continental average is shown in Fig. 1. The maps are oriented so that the PP is along the x-axis. The horizon is the circle with radius 90° around the zenith at the origin. The sun is located in the right half of the map, the aureole is clearly visible in the *I*-component.

There exists one fundamental difference between the conventions of all-sky imaging and RT modeling, which has adopted the convention of the scanning method. For a sky-scanning instrument, the reference angle for the Stokes vector rotates along with the viewing direction, i.e. 0° angle of polarization is always the same in the instrument reference frame (e.g. perpendicular) and will be equal to the azimuth angle when projected onto the plane. In the imaging method (using a rotating polarizer in the image plane), the Stokes reference angle depends on the polarizer offset angle and is constant across the image plane.

The Stokes maps must therefore be transformed to allow comparison of imaging and sky scanning method or model output. The transformation from the co-rotating to fixed reference frame is realized by a linear transformation, the 2×2 rotation matrix with rotation angle 2φ, where φ is the azimuth:

$$\begin{pmatrix} Q_\mathrm{r} \\ U_\mathrm{r} \end{pmatrix} = \begin{pmatrix} \cos 2\varphi & \sin 2\varphi \\ -\sin 2\varphi & \cos 2\varphi \end{pmatrix} \begin{pmatrix} Q \\ U \end{pmatrix} \quad (2)$$

The first Stokes component (the radiance *I*) is unaffected by the transformation. Q_r and U_r are the rotated Stokes parameters that will naturally be measured with a polarized

AMTD
5, 8815–8838, 2012

all-sky imager. The transformed maps are shown in Fig. 2. Note that that the rotated maps are smooth over the projection, and the singularity at the zenith is eliminated by the transformation. This will be a useful advantage for the image analysis in the next section.

Finally, we normalize the Stokes components Q_r and U_r with the radiance I at each pixel, so we consider the relative quantities Q_r/I andU_r/I. The resulting relative Stokes maps from the above example are shown in Fig. 3. This has two distinct advantages, especially when using a commercial digital camera for imaging.

First, absolute radiometric calibration is elaborate, has to be performed regularly and typically requires temperature stabilization in field operation. Even then, the calibration accuracy is of the order of 5 %. Second, the aureole is generally difficult for analysis because the large difference of direct sun irradiance and sky radiance, leading to overexposed pixels and saturation effects. The direct sun can be shaded by a mechanical sun-occulter to avoid these problems, but the information from the aureole is lost nonetheless. In the normalized Stokes maps, the aureole is weighted least and is naturally eliminated.

2.2 Image analysis

The next question we address is the efficiency of data representation in the Stokes maps, to make it more feasible for a retrieval algorithm. The data considered here, involve two relative Stokes maps at two wavelengths, i.e. minimum of 35×35 pixels $\times 2 \times 2$, of the order of 10^3 data points. The original data from digital photos will be even higher by a factor of more than 100. This number is neither efficient in data representation, nor is it tractable for an inverse problem involving optimization.

Any function can be represented as coefficients of basis functions, such as a Fourier series. For the hemispherical projections considered here, 2-D functions, such as the Zernike polynomials are well suited. Zernike polynomials define an orthonormal basis on the unit disk and are commonly used in applied optics to describe imaging distortions (Born and Wolf, 1999). The Zernike polynomials are indexed by two integers, n

AMTD
5, 8815–8838, 2012

and m, associated with radial and azimuthal degrees of freedom. Here we use a single ordering number, derived by first sorting the radial, then the azimuthal number. The first orders correspond to (n,m): (0,0), (1,−1), (1,1), (2,−2), (2,0), etc.

By describing the relative Stokes maps Q_r/I and U_r/I in terms of the first few Zernike coefficients (ZC), we can considerably reduce the number of independent measurement parameters. The first ten ZC are shown in Fig. 4.

Note that the ZC of the Q_r/I maps and U_r/I maps are mutually orthogonal in the sense that vanishing ZC of the Q_r/Imaps are not vanishing for the U_r/I maps, and vice versa. This is because the maps of Q_r/I and U_r/I are symmetric and anti-symmetric, respectively, about the principal plane. This means that the two ten-component vectors of ZC can simply be added, which is equivalent to the first ten ZC of the sum of the maps $(Q_r + U_r)/I$.

Since different aerosol types are not expected to change the Stokes maps on a small spatial scale, we consider the first ten coefficients, describing the characteristic shape. The higher the Zernike order, the more nodes are exhibited by the functions and hence the more sensitive the ZC to small scale changes. A more rigorous justification of this cut-off will be possible after investigating some aerosol scenarios and will be presented in the discussion section.

Including the ZC of our second wavelength at 450 nm, we have a 20-component vector representing our data. In pattern recognition and machine vision research, such a measurement vector is commonly called feature vector (FV), a term we will also adopt in this work. This feature vector can be directly used for aerosol property retrieval, e.g. the AERONET retrieval algorithm.

2.3 Aerosol scenarios

To investigate the general feasibility for retrieval of aerosol properties, we model the polarized radiance distributions for different possible aerosol scenarios (sometimes also called synthetic data) and generate the corresponding FVs, which span the so-called

AMTD
5, 8815–8838, 2012

FV-space. The FV-space is related to the a priori information, which always plays a part in the retrieval process (Dubovik et al., 2000).

As a simple FV space we first consider the aerosol components given in OPAC: water soluble (WASO), insoluble (INSO), SOOT, mineral accumulation mode (MIAM), sea salt accumulation mode (SSAM). In the aerosol input file we assume a constant number density for all components up to height of 5 km. We model the Stokes maps for three different scaling factors of AOD. The resulting FV space, consisting of $3 \times 5 = 15$ FVs, is shown as a matrix in Fig. 5. The absolute values for the FV components for each OPAC aerosol decrease with increasing AOD, which can be understood as a decrease of the degree of polarization with increased aerosol scattering.

The FV space is a multivariate distribution, showing significant correlation between its components. This is because the characteristic shape of the Stokes maps is largely invariant under the influence of different aerosol components and mainly the amplitude changes, affecting all ZC in a similar way. Considering this correlation, the number of independent parameters in the FV can be further reduced. The rotation matrix that diagonalizes the covariance matrix of the FV space projects each FV onto the so-called principal axes. The eigenvalues of the rotation matrix are the variances along each axis. In case of high correlation, most eigenvalues are close to zero and only the first few coordinates in this transformed coordinate system have to be considered. This is a common tool in statistical analysis, called principal component analysis (PCA).

First, the FV components are standardized so that the mean of the distribution of each component is zero. The standard deviation is not normalized to unity since the absolute and not the relative errors of the FV components are roughly constant. The diagonalization and calculation of principal components (PC) is performed within the standard statistics toolbox of Matlab.

We find that the first two PCs relate to 99 % of the total variance. So the 20-dimensional FV can be projected onto a plane in two dimensions with the highest variances, with the first two PCs being the new coordinates.

AMTD
5, 8815–8838, 2012

In this plane, shown in Fig. 6, each aerosol component traces a line originating at a common point with AOD zero (Rayleigh atmosphere) and extending into different directions with increasing AOD. As a reference, the blobs indicate AOD = 0.2 at 450 nm. Concentrating on these reference points of constant AOD, one can notice the effect of different size and single scatter albedo (SSA) of each aerosol component. The size is characterized by the effective radius of the lognormal size distribution with respect to volume. The SSA is a dimensionless quantity defined as the ratio of scattering optical depth to total optical depth (scattering plus absorption).

SOOT for example, as given by OPAC, has a relatively small effective radius of 0.05 µm and a low SSA of 0.23, having almost no influence on the FV. Absorption affects Q, U and I similarly, while scattering might increase I but decrease Q or U if the scattered light is unpolarized. The WASO type has about double the effective radius as SOOT but a much higher SSA of 0.97. Types INSO and MIAM are both large radius particles with SSA = 0.72 and 0.83, respectively, and their trajectories are aligned, with MIAM extending further out due to its higher SSA.

In reality, however, the atmosphere most likely contains a mixture of components, typically exhibiting bimodal lognormal size distributions, with a fine and a coarse mode. Representative mixtures are given in the OPAC base, e.g. continental average, continental polluted, urban or desert. The average continental, polluted continental and urban mixtures consist of WASO, INSO and SOOT with respective increasing total amount of particles and increasing mixing ratio of soot. The respective AODs are 0.15, 0.33 and 0.64 at 550 nm. These three mixtures are fine-mode dominated whereas the desert type aerosol mixture is coarse mode dominated and consists predominantly of WASO, MIAM and mineral nucleation mode (MINM) with AOD 0.3 at 550 nm.

We modeled the Stokes maps of each of the above aerosol mixtures and project their FV onto the first two principal axes, as previously determined, and added the points in the plot in Fig. 6. In the PC coordinates, the continental and urban mixtures appear close to the WASO trajectory, but separated along the line due to different AOD. So

AMTD
5, 8815–8838, 2012

this representation is insensitive to the soot fraction in fine mode dominated aerosol mixtures.

The desert mixture appears between the WASO and the MIAM trajectory, as expected from its constituents. However, it almost coincides with the SSAM trajectory. So bimodal coarse aerosols and mono modal aerosols with a slightly smaller effective radius would be ambiguous in a retrieval scheme based on this representation.

However, inverting sky radiance measurements only, to unambiguously characterize aerosols is an inherently ill-posed problem, and some a priori assumptions are needed to constrain the solutions (Dubovik et al., 2000). So in the next step, we take the AOD as given and assume a bimodal size distribution.

As an alternative basis of FVs we consider two bimodal size distributions, one coarse mode, and one fine mode dominated with varying scattering and absorbing properties. We consider two distinct types of aerosol mixtures from OPAC, desert and urban. In terms of size distributions, these two types are two extreme examples with respect to typical continental aerosols. In addition to their size distribution, aerosols are characterized by their SSA. In the model input, we scaled the SSA for both wavelengths from 0.7–0.95 (in steps of 0.05) covering the range of typically occurring values. In these scenarios we hold the AOD constant at 0.2 at 450 nm. So in this case AOD is assumed to be given by an independent sun photometer measurement and is not a parameter for the retrieval.

The resulting FV space is spanned by 12 vectors, corresponding to six different SSA for each size distribution. Again we project the FV space onto the plane of the two highest variances, shown in Fig. 7.

To gauge the distance between the points they have to be compared with the measurement error. Since the PCs are indirectly derived from an integral over the different shapes of the Zernike functions, analytical error propagation is not suitable here and we estimate the measurement error in PC space by a Monte-Carlo method. We add random, Gaussian noise to the modeled radiances and simulate the complete

AMTD
5, 8815–8838, 2012

measurement process, i.e. computing I_0, I_{45}, I_{90} and I_{135} and deriving the I, Q and U. Then we rotate the 50 generated FVs into PC space.

A statistical error of 10 % of the lowest intensity (which coincides at about 90° scattering angle) has been added as random pixel noise. The resulting relative error is only around 2 % for the first two FV components and in PC space corresponds to an SSA difference of less than 0.05. So the FV is highly insensitive to pixel noise from the original camera images, because the Zernike coefficients are a weighted sum of the whole image, where statistical noise is averaged out.

The points in Fig. 7 are plotted with size corresponding to about the 1-sigma uncertainty. So the points of different size distribution and SSA are indeed well separated by more than the measurement error, indicating that the aerosol characterization with respect to these two parameters is feasible.

As a simple retrieval test, we generate an OPAC continental average scenario with AOD of 0.2 at 450 nm, calculate the corresponding FV and use the rotation matrix from above to project it onto the principal axes. The data point is plotted in Fig. 7 and appears close to the urban size distribution (i.e. fine mode dominated) with a high SSA of 0.95, compared to the true SSA of 0.93.

Finally, we generate the same FV space for a SZA of 30°, again varying the SSA for two bimodal size distributions (see Fig. 8). The points for different SSA are still well separated, indicating that the method also works for lower SZA. Note that the range of the larger variance (first PC on the x-axis) is about the same as for 60° SZA, but the range of the second PC is reduced. This corresponds to a slight decrease in information content of a measured FV and is a result of a reduction of observable scattering angles in the sky.

In particular, the range of scattering angles in the almucantar decreases at lower SZA and retrieval schemes considering sky radiance measurements in the almucantar become more difficult (Dubovik et al., 2000) which imposes a limit on the observation schedule. The standard AERONET operation includes almucantar measurements at a minimum of about 54° SZA (aimass 1.7).

AMTD
5, 8815–8838, 2012

3 Discussion

We have introduced a FV based on the first ten ZC. As a justification for this cut-off we show that the information content of the FV is satisfactorily captured. The information content can be defined as the logarithm of ratios of the a priori and posteriori state space volumes (Rodgers, 2000). In our 2-D PC representation this is proportional to the area spanned by the FV space (a priori), considering a constant posteriori area (measurement error). Figure 9 shows the increasing information content for the FV (FV-space for OPAC components) with increasing ZC, leveling off after ten components per wavelength.

Regarding the second FV-space of two bimodal size distributions with variable SSA, we agree that the modeling is not necessarily physically realistic. One problematic issue is the scaling of SSA in MYSTIC. This scaling changes only the absorption while leaving the phase function unchanged. This methodology is highly convenient in our case, it may be, however, unphysical for aerosol microphysical properties. It would be more appropriate to manipulate the aerosol input parameters on the microphysical scale, the complex index of refraction. Increasing the imaginary part of the index of refraction leads to a decrease in SSA and possibly a different phase function. In this first study we target the SSA as a retrieval goal as it is one of the most relevant quantities with respect to aerosol direct radiative effects.

These issues will result in a modified shape of our FV space, which does not weaken our conclusion. This article is mainly aimed at showing the proof-of-principle for the method, and a proper retrieval scheme will be implemented in the future. In fact, the maximum likelihood estimation method that has been implemented in the AERONET scheme could be adopted without modification.

An efficient optimization procedure can only be implemented with a fast forward model. For the forward modeling to generate the FV introduced here a considerable short cut has been suggested (R. Buras, personal communication, 2012). Instead of calculating the polarized radiances for each viewing angle, and hence the ZC, the ZC

AMTD
5, 8815–8838, 2012

can be calculated directly by weighting the random photon directions in the MC-model with the Zernike polynomials. This would allow a tractable forward modeling for the optimization problem. Alternatively, considering the compact representation of two PCs, a simple look-up table scheme would also be possible.

When implementing this scheme with real all-sky images, flare reflections, dirt on the objective and obstacles on the horizon will create artifacts in ZC. These problems should be handled by modern image processing techniques. Also the broadband wavelength response of typical sensors should be addressed by respective filtering.

Finally, it is noted that cloud cover information is intrinsically included in the all-sky images and automatically extracting the cloud cover is straight-forward (Kreuter et al., 2009). Scattered clouds outside the PP or almucantar are a possible error source for the sky scanning method, since the retrieval always assumes clear sky. By 3-D modeling the cloud scene, the imaging technique may extend retrieval possibilities to certain cloudy sky scenes.

4 Conclusions

We have proposed a 20-dimensional measurement vector (feature vector) derived from polarized all-sky images. This feature vector consist of the Zernike coefficients of relative Stokes maps and is ideal to accommodate common problems associated with all-sky imaging: the aureole, absolute calibration and pixel noise.

Using a RT model, we generated FV spaces for possible aerosol scenarios using the OPAC aerosols as basis. Considering the covariance of the FV spaces we projected the FV onto the first two principal axes with the highest variances, allowing a two dimensional representation.

We have shown that in principle, using this method, aerosol types can be distinguished with respect to two bimodal size distributions (coarse mode and fine mode dominated) and SSA with an accuracy better than 0.05 at an AOD of 0.2 at 450 nm.

AMTD
5, 8815–8838, 2012

Based on this work, a proper retrieval algorithm can be implemented in the future. Polarized all-sky imaging is a feasible and simple method for aerosol characterization, especially in combination with a sun photometer.

Acknowledgements. We thank C. Emde and R. Buras for many helpful discussions regarding RT modeling and the use of MYSTIC.

References

Boesche, E., Stammes, P., Ruhtz, T., Preusker, R., and Fischer J.: Effect of aerosol microphysical properties on polarization of skylight: sensitivity study and measurements, Appl. Optics, 45, 8790—8805, 2006.

Born, M. and Wolf, E.: Principles of Optics, 7th Edn., Cambridge, UK, Cambridge University Press, 1999.

Cazorla, A., Shields, J. E., Karr, M. E., Olmo, F. J., Burden, A., and Alados-Arboledas, L.: Technical Note: Determination of aerosol optical properties by a calibrated sky imager, Atmos. Chem. Phys., 9, 6417–6427, doi:10.5194/acp-9-6417-2009, 2009.

Dubovik, O. and King, M. D.: A flexible inversion algorithm for retrieval of aerosol optical properties from sun and sky radiance measurements, J. Geophys. Res., 105, 20673–20696, 2000.

Dubovik, O., Smirnov, A., Holben, B. N., King, M. D., Kaufman, Y. J., Eck, T. F., and Slutsker, I.: Accuracy assessment of aerosol optical properties retrieved from Aerosol Robotic Network (AERONET) Sun and Sky radiance measurements, J. Geophys. Res., 105, 9791–9806, 2000.

Emde, C., Buras, R., Mayer, B., and Blumthaler, M.: The impact of aerosols on polarized sky radiance: model development, validation, and applications, Atmos. Chem. Phys., 10, 383–396, doi:10.5194/acp-10-383-2010, 2010.

Forster, P., Ramaswamy, V., Artaxo, P., et al.: Changes in Atmospheric Constituents and in Radiative Forcing, in: Climate Change 2007: The Physical Science Basis. Contribution of WG I to the Fourth AR of the IPCC, Cambridge University Press, Cambridge, United Kingdom and New York, NY, USA, 2007.

Hess, M., Koepke, P., and Schult, I.: Optical Properties of Aerosols and Clouds: The Software Package OPAC, B. Am. Meteorol. Soc., 79, 831–844, 1998.

AMTD

5, 8815–8838, 2012

Holben, B. N., Eck, T. F., Slutsker, I., Tanre, D., Buis, J. P., Setzer, A., Vermote, E., Reagan, J. A., Kaufman, Y. J., Nakajima, T., Lavenu, F., Jankowiak, I., and Smirnov, A.: AERONET – A federated instrument network and data archive for aerosol characterization, Remote Sens. Environ., 66, 1–16, 1998.

Kaufman, Y. J., Tanré, D., and Boucher, O.: A satellite view of aerosols in the climate system, Nature, 419, 215–223, 2002.

Kreuter, A., Zangerl, M., Schwarzmann, M., and Blumthaler, M.: All-sky imaging: a simple and versatile system for atmospheric research, Appl. Optics, 48, 1091–1097, 2009.

Kreuter, A., Emde, C., and Blumthaler, M.: Measuring the Influence of Aerosols and Albedo on Sky Polarization, Atmos. Res., 98, 363–367, 2010.

Li, Z., Goloub, P., Dubovik, O., Blarel, L., Zhang, W., Podvin, T., Sinyuk, A., Sorokin, M., Chen, H., Holben, B., Tanre, D., Canini, M., and Buis, J.-P.: Improvements for ground-based remote sensing of atmospheric aerosol properties by additional polarimetric measurements, J. Quant. Spectrosc. Ra., 110, 1954–1961, 2009.

Liu, Y. and Voss, K.: Polarized radiance distribution measurement of skylight. II. Experiment and data, Appl. Optics, 36, 8753–8764, 1997.

Mayer, B.: Radiative transfer in the cloudy atmosphere, Euro. Phys. J. C, 1, 75–99, 2009.

Mayer, B. and Kylling, A.: Technical note: The libRadtran software package for radiative transfer calculations – description and examples of use, Atmos. Chem. Phys., 5, 1855–1877, doi:10.5194/acp-5-1855-2005, 2005.

North, J. A. and Duggin, M. J.: Stokes vector imaging of the polarized sky-dome, Appl. Optics, 36, 723–730, 1997.

Pust, N. J. and Shaw, J. A.: Digital all-sky polarization imaging of partly cloudy skies, Appl. Optics, 47, H190–H198, 2008.

Rodgers, C. D.: Inverse methods for atmospheric sounding, Theory and Practice, University of Oxford, UK, 2000.

Vermeulen, A., Devaux, C., and Herman, M.: Retrieval of the Scattering and Microphysical Properties of Aerosols from Ground-Based Optical Measurements Including Polarization. I. Method, Appl. Optics, 39, 6207–6220, 2000.

AMTD
5, 8815–8838, 2012

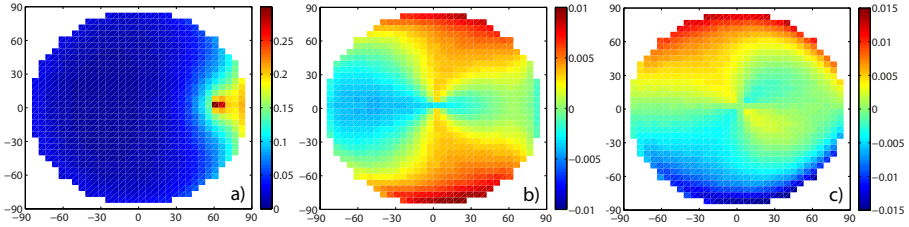

Fig. 1. Stokes maps *I* **(a)**, *Q* **(b)** and *U* **(c)** from model calculations for 650 nm, 60° SZA and OPAC continental average aerosol with AOD 0.2 at 450 nm. The radiance values are normalized to the extraterrestrial irradiance.

AMTD
5, 8815–8838, 2012

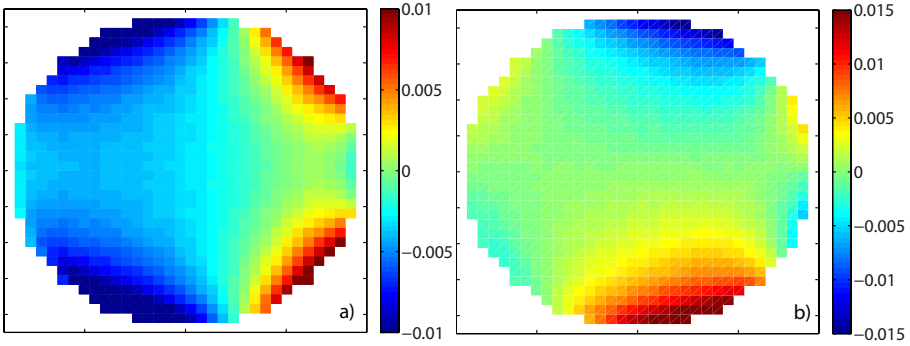

Fig. 2. Rotated Stokes maps for the same model calculations as in Fig. 1: **(a)** Q_r and **(b)** U_r. Axes are the same as in Fig. 1.

AMTD
5, 8815–8838, 2012

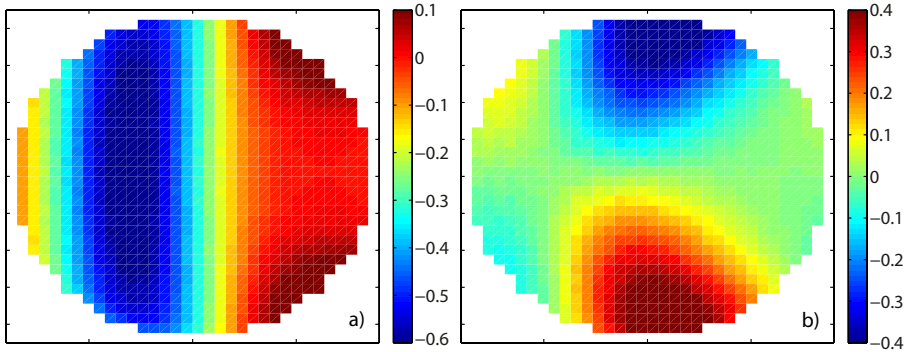

Fig. 3. Relative rotated Stokes maps for the same model calculations as in Fig. 1: **(a)** Q_r/I and **(b)** U_r/I. Axes are the same as in Fig. 1.

AMTD
5, 8815–8838, 2012

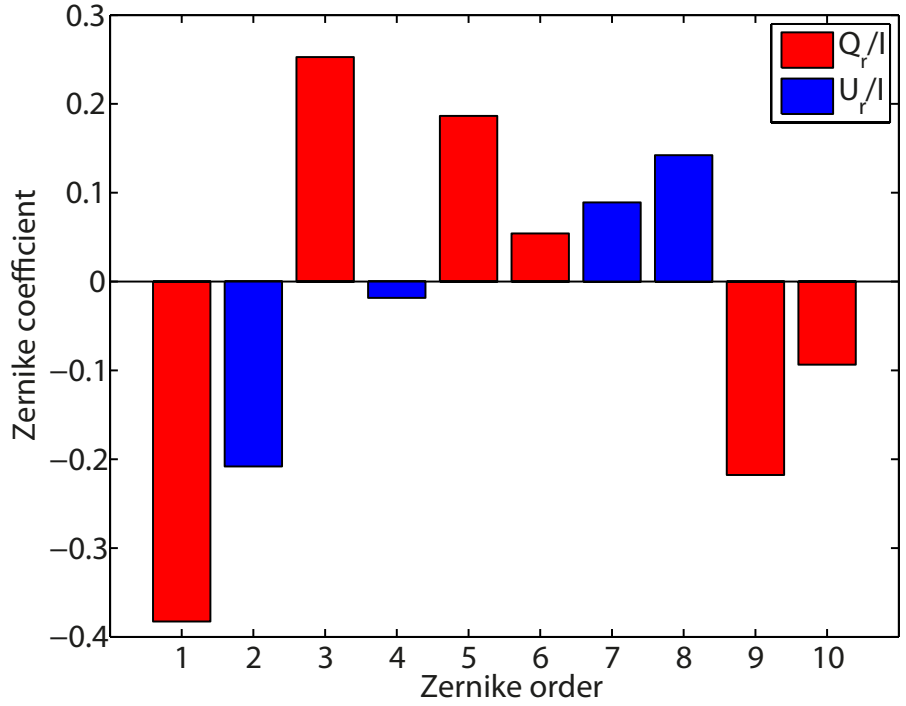

Fig. 4. First ten Zernike coefficients for Q_r/I and U_r/I. The sum defines the feature vector for 650 nm.

AMTD
5, 8815–8838, 2012

Feasibility of polarized all-sky imaging

A. Kreuter and
M. Blumthaler

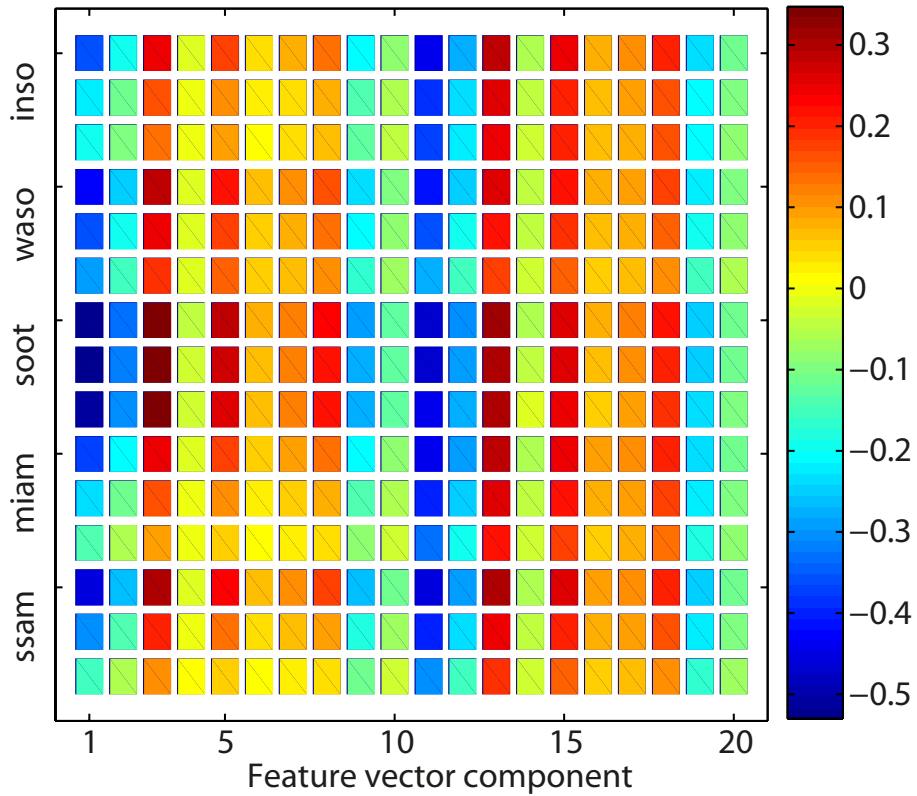

Fig. 5. Feature vector space for OPAC aerosol components: rows correspond to FVs for inso, waso, soot, miam and ssam, for three different AOD scalings (top to bottom, respectively). FV-components 1–10 correspond to 650 nm and components 11–20 to 450 nm.

AMTD
5, 8815–8838, 2012

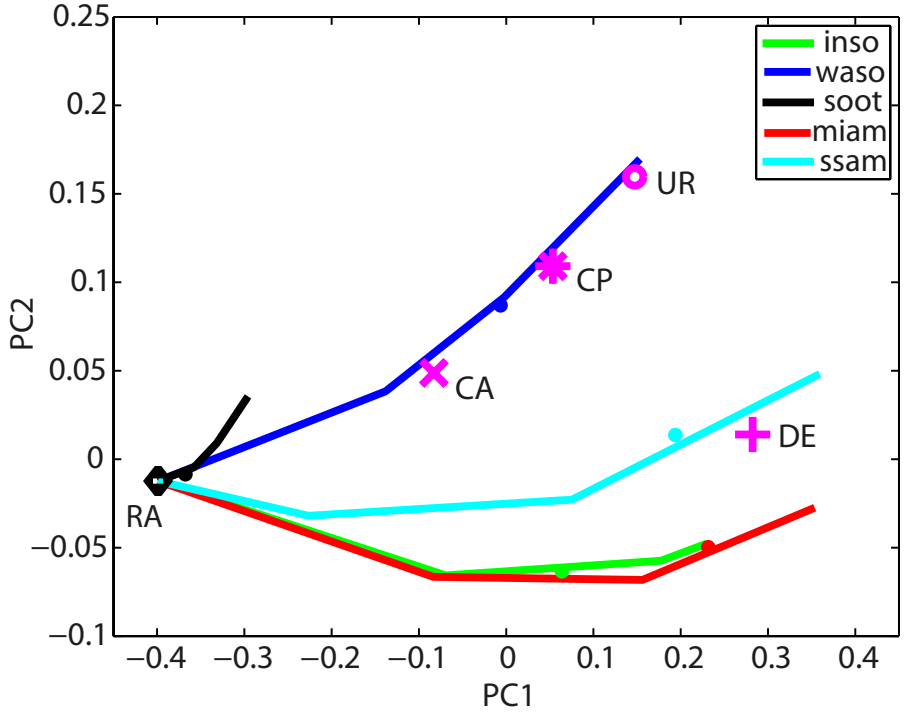

Fig. 6. First two principal components of the FV space for OPAC aerosol components. The AOD has been scaled, AOD = 0.2 at 450 nm is indicated as blobs. All trajectories originate at AOD = 0 corresponding to a pure Rayleigh atmosphere (RA). Aerosol mixtures continental average (CA), continental polluted (CP), urban (UR) and desert (DE) are shown.

AMTD
5, 8815–8838, 2012

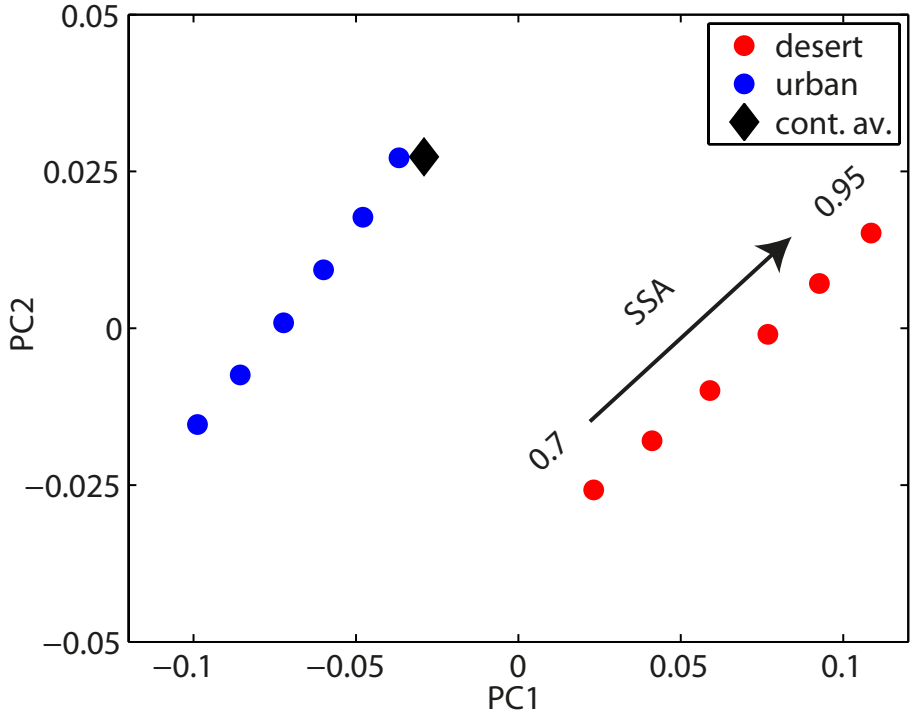

Fig. 7. First two principal components of the FV space for two different size distributions and scaled SSA at 60° SZA. The size of the data points correspond to about a 1-sigma uncertainty, derived from invoking a 10 % absolute pixel noise and simulating the measurement process.

AMTD
5, 8815–8838, 2012

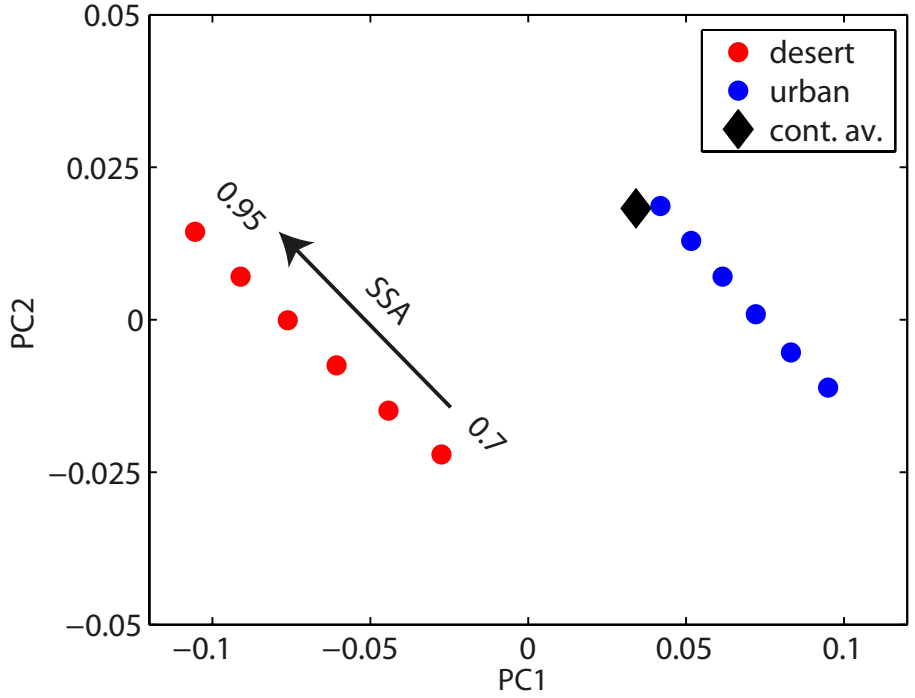

Fig. 8. Same as Fig. 7, but for 30° SZA. First two principal components of the FV space for two different size distributions and scaled SSA.

AMTD
5, 8815–8838, 2012

Feasibility of polarized all-sky imaging

A. Kreuter and M. Blumthaler

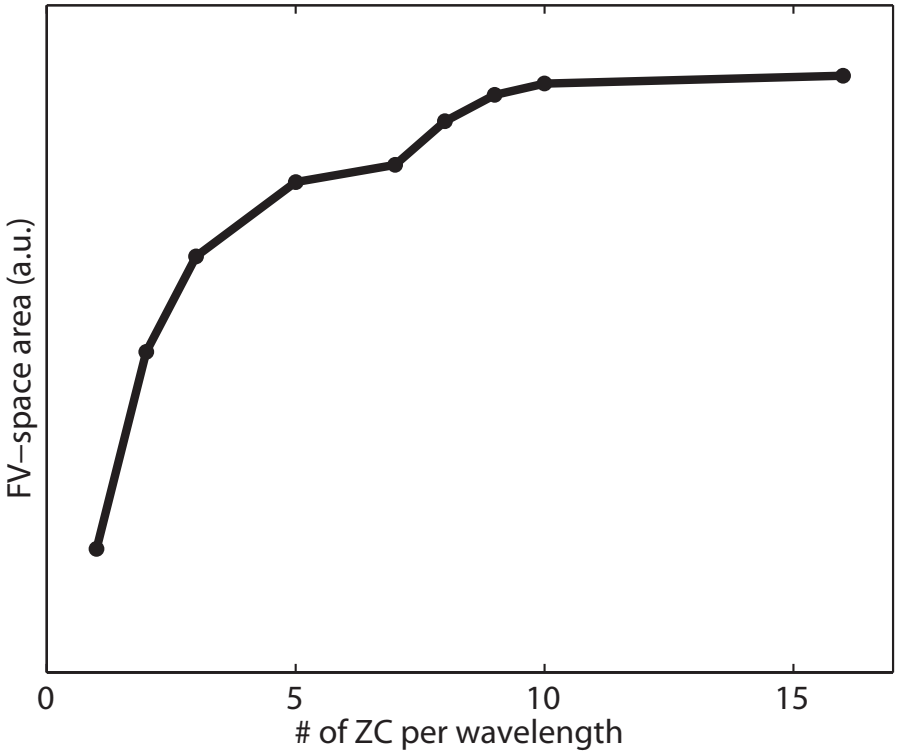

Fig. 9. Area of spanned OPAC FV-space as a measure for the information content of the FV vector as function of number of used ZC.

AMTD
5, 8815–8838, 2012